

Data-Driven Design of NASICON-Type Electrodes Using Graph-Based Neural Networks

Yoonsu Shim,^[a] Incheol Jeong,^[b] Junpyo Hur,^[a] Hyoungjeen Jeen,^[d] Seung-Taek Myung,^[e] Kang Taek Lee,^[b, c] Seungbum Hong,^[a] Jong Min Yuk,*^[a] and Chan-Woo Lee,*^[f]

Sodium superionic conductor (NASICON)-type cathode materials are considered promising candidates for high-performance sodium-ion batteries (SIBs) because of the abundance and low cost of raw materials. However, NASICON-type cathodes suffer from low capacities. This limitation can be addressed through the activation of sodium-excess phases, which can enhance capacities up to theoretical values. Thus, this paper proposes the use of transition metal (TM)-substituted $\text{Na}_3\text{V}_2(\text{PO}_4)_3\text{F}_3$ (NVPF) to induce sodium-excess phases. To identify suitable doping elements, an inverse design approach is developed, combining machine learning prediction and density functional

theory (DFT) calculations. Graph-based neural networks are used to predict two crucial properties, i.e., the structural stability and voltage level. Results indicate that the use of TM-substituted NVPF materials leads to about 150% capacity enhancement with reduced time and resource requirements compared with the direct design approach. Furthermore, DFT calculations confirm improvements in cyclability, electronic conductivity, and chemical stability. The proposed approach is expected to accelerate the discovery of superior materials for battery electrodes.

1. Introduction

Sodium-ion batteries (SIBs) have emerged as promising alternatives to lithium-ion batteries (LIBs) because of the abundance and low cost of raw minerals. However, challenges remain in addressing the low energy density and instability during cycling. The sodium-ion storage capacity can be enhanced by developing improved cathode materials. Recently, sodium superionic conductor (NASICON)-type materials, including $\text{Na}_3\text{V}_2(\text{PO}_4)_3\text{F}_3$ (NVPF), $\text{Na}_3\text{V}_2(\text{PO}_4)_3$, and $\text{Na}_3\text{V}(\text{PO}_4)_2\text{F}_2$, have been reported as potential candidates in this context. Among these materials, NVPF exhibits the highest theoretical capacity of 128 mAh/g and has thus garnered significant interest. However, improvements are warranted to address the low sodium-ion storage capacity, low electronic conductivity, and high cost of vanadium raw minerals.^[1]

Despite efforts to enhance energy density and cost efficiency by substituting vanadium ions with other transition metal (TM) ions, such as Ti, Mn, Fe, and Y in NVPF cathodes,^[2–6]

it remains necessary to identify suitable TM-substituted NVPF (NMPF) candidates to optimize the electrochemical properties. In particular, exploring TM binary combinations offers the potential to discover numerous promising candidates. However, TM-substitution strategies are time- and resource-intensive owing to the large number of candidates to be explored experimentally and the necessity of screening materials by density functional theory (DFT) calculations. To overcome these challenges, an inverse design approach based on big data and machine learning (ML) must be incorporated, enabling more rapid and efficient assessment of electrochemical properties.

Specifically, the inverse design approach can specify the structure and composition of materials considering the target performances by using big data and ML models to identify correlations between the property and structural spaces of materials.^[7–12] Among such models, graph-based neural networks (GNNs) have demonstrated success in efficiently predicting the properties of novel materials from their atomic structure, based on DFT calculations. Various GNN models, such

[a] Dr. Y. Shim, J. Hur, Prof. Dr. S. Hong, Prof. Dr. J. M. Yuk
Department of Materials Science and Engineering, Korea Advanced Institute of Science and Technology, Daejeon 34141, Republic of Korea
E-mail: jongmin.yuk@kaist.ac.kr

[b] Dr. I. Jeong, Prof. Dr. K. T. Lee
Department of Mechanical Engineering, Korea Advanced Institute of Science and Technology, Daejeon 34141, Republic of Korea

[c] Prof. Dr. K. T. Lee
Department of Mechanical Engineering, Korea Advanced Institute of Science and Technology, Daejeon 34141, Republic of Korea

[d] Prof. Dr. H. Jeen
Department of Physics, Pusan National University, Busan, 46241, Republic of Korea

[e] Prof. Dr. S.-T. Myung
Hybrid Materials Research Center, Department of Nanotechnology and Advanced Materials Engineering & Sejong Battery Institute, Sejong University, Seoul 05006, Republic of Korea

[f] Dr. C.-W. Lee
Energy AI & Computational Science Laboratory, Korea Institute of Energy Research, Daejeon 34129, Republic of Korea
E-mail: cwandtj@kier.re.kr

 Supporting information for this article is available on the WWW under <https://doi.org/10.1002/batt.202400186>

 © 2024 The Authors. *Batteries & Supercaps* published by Wiley-VCH GmbH. This is an open access article under the terms of the Creative Commons Attribution Non-Commercial NoDerivs License, which permits use and distribution in any medium, provided the original work is properly cited, the use is non-commercial and no modifications or adaptations are made.

as CGCNN,^[13] MT-CGCNN,^[14] MEGNet,^[15] ElemNet,^[16] GATGNN,^[17] ICGCNN^[18] and CrysXPP,^[19] have been developed for crystal property prediction. Grossman *et al.* screened promising candidates of dendrite-suppressed solid electrolytes by predicting shear and bulk moduli from the CGCNN framework.^[20] Shenoy *et al.* developed a deep learning approach incorporating transfer learning based on the MEGNet architecture to predict key properties of point defects in two-dimensional materials and identified promising and previously unexplored dopant defect structures.^[21] Therefore, the GNN model can also be a valuable approach to efficiently design the TM-substituted NMPF efficiently to improve the energy density of SIBs.

Building upon the existing work, we use a GNN-assisted high-throughput method to establish a structure–property correlation map. The GNN models are trained and tested using DFT datasets and output noble sodium-excess NMPF materials with excellent properties including high capacity, electronic conductivity, and stability.

2. Methods

2.1. Computational Details

All calculations were performed using the Vienna Ab initio Simulation Package (VASP),^[22] adopting the projector-augmented wave (PAW) scheme with spin-polarization, following the Perdew–Burke–Ernzerhof (PBE) formulation.^[23] A cutoff energy of 550 eV was set for the plane-wave expansion of wave functions, and a *k*-point grid of 1×1×1 was used with the Monkhorst–Pack method^[24] until the forces on each atom converged to less than 0.01 eV/Å (energy per atom). The total ground-state energies converged within 1.0×10⁻⁶ eV. The projected density of states (PDOS) was determined using fine 4×4×4 *k*-point grids. Hubbard U terms were used to model each substitution atom, including vanadium ions. The pseudo-potential, Hubbard U terms, and correction energy for each element were defined following the methodology specified by the Materials Project,^[25] as outlined in Table S3. Hybrid functional (HSE06) calculations were performed to prevent the underestimation of the bandgap, typical in the generalized gradient approximation (GGA) functional. To reduce computational costs, we first determined *k*-points corresponding to the valence band maximum and conduction band minimum using the GGA(+U) functional. Subsequently, one-shot hybrid functional calculations were performed on the *k*-points of these band-edges.^[26] The crystal orbital Hamiltonian population (COHP) was calculated directly from the plane-wave output using the LOBSTER program.^[27]

The formation energy, E_{form} , is defined as

$$E_{\text{form}} = E_{\text{system}} - \sum_i N_i \mu_i, \quad (1)$$

where E_{system} is the DFT energy of the compound; and N_i and μ_i denote the number of atoms and chemical potential of species

i, respectively. The chemical potential values were derived from the Materials Project database,^[25] as indicated in Table S3.

2.2. Deep Learning

Pretrained models derived from MEGNet^[15] were used in this study. The MEGNet models were constructed using the Keras API^[28] and TensorFlow backend.^[29] All material data used for training and test were randomly split into an 0.8:0.2 ratio using the scikit-learn package.^[30] The final dataset involved 1,171 structures, with all unary datasets included in the training set to ensure elemental diversity. The models were trained using the ADAM optimizer, mean-square-error (MSE) loss function, learning rate of 0.001, and batch size of 128. Structure graphs were generated using graph convertors in the MEGNet module.

2.3. Prediction of Synthesizability

The synthesizability of candidate materials was predicted using a partially supervised protocol under the positive and unlabeled machine learning (PU learning) scheme, with CGCNN implemented as the classifier.^[31] The number of iterations for bootstrap aggregating was 100. The source codes are available on the GitHub repository (<https://github.com/kaist-amsg/Synthesizability-PU-CGCNN>).

3. Results and Discussion

3.1. Workflow of the Inverse Design Approach

Two key approaches can be used for material discovery: the Edisonian approach and inverse design approach. The Edisonian approach begins with structure design through modeling or synthesis, followed by property studies using theoretical calculations or experimental measurements. The Edisonian approach suffers from significant drawbacks, including risk of failure and inefficient use of resources. In contrast, the inverse design approach starts with the targeted desired properties, followed by the search for ideal structures exhibiting the best performance. One form of inverse design is high-throughput screening, involving extensive explorations of all possible structure and property spaces.^[8] However, this approach is time- and resource-intensive. Therefore, in this study, an ML approach is combined with GNNs to facilitate high-throughput screening. The process flow of the GNN-assisted high-throughput method for discovering novel electrode materials is illustrated in Figure 1 and involves the following key steps:

- (1) Generating atomic structures of NMPFs.
- (2) Acquiring DFT formation energies from the NMPF atomic structures.
- (3) Constructing a ML model using a GNN model

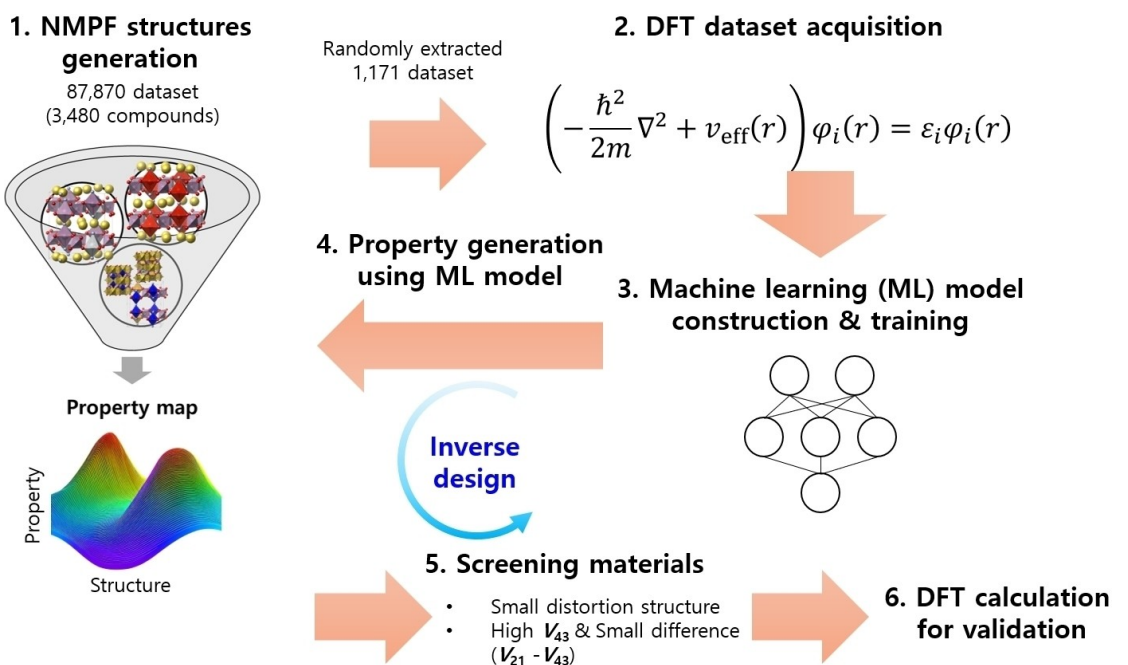


Figure 1. Process flow of inverse design.

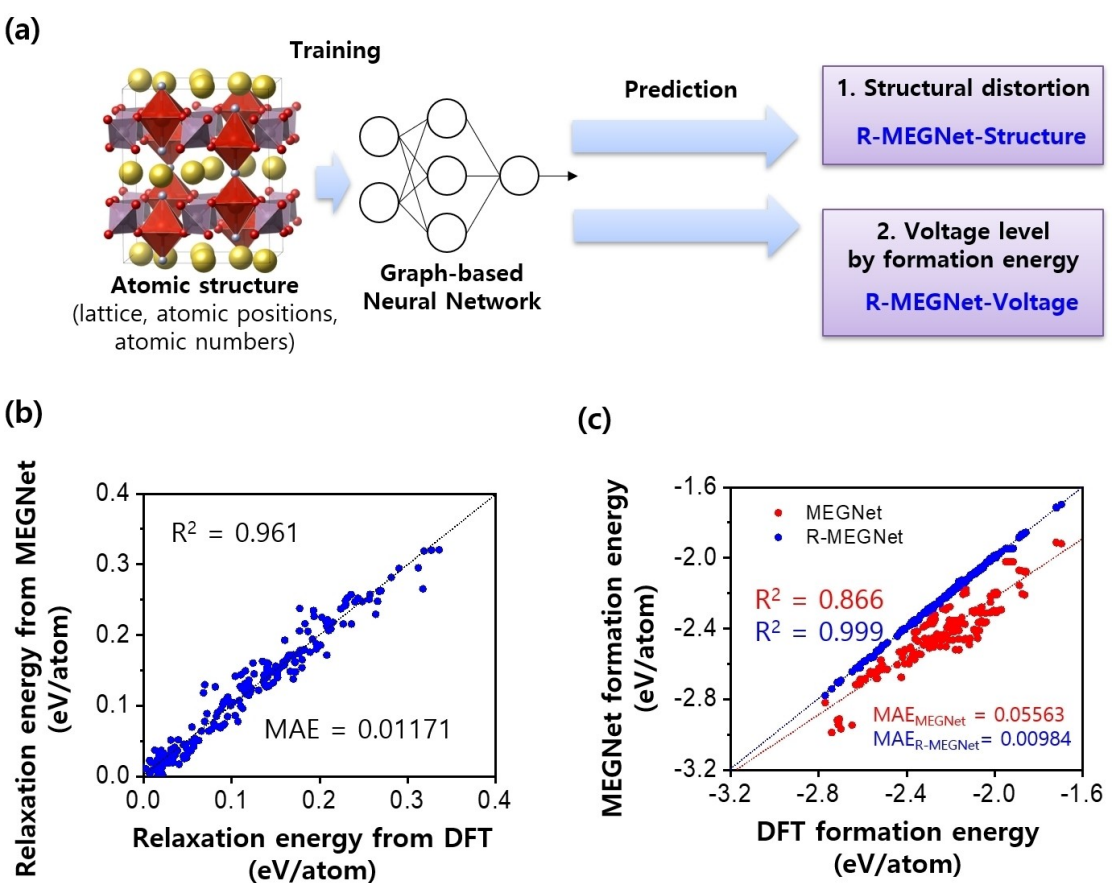


Figure 2. Two types of graph-based neural networks for predicting structural distortion and voltage level. Parity plots of trained models for (b) structure distortion and (c) voltage level prediction. Red and blue points correspond to the original MEGNet and R-MEGNet models, respectively.

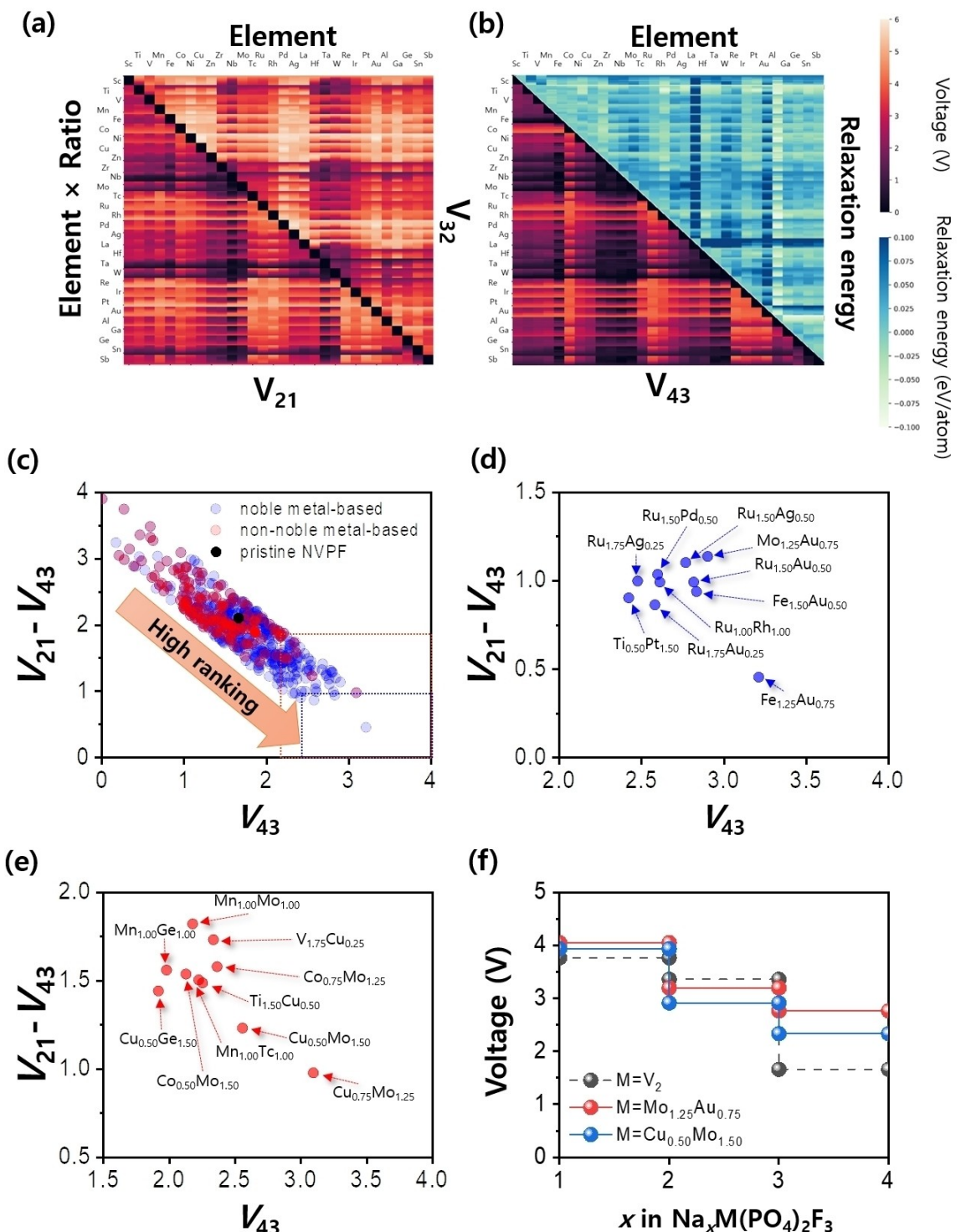


Figure 3. Property spaces of (a) V_{21} and V_{32} levels, and (b) V_{43} level and the relaxation energy with respect to transition metal (TM) elements. The x-axis presents the substitution elements, and the y-axis presents the substitution elements and composition ratio. (c) Screening results and ranking of bi-substituted NMPF structures composed of 30 transition metal elements. Enlarged diagrams of top-10 (d) noble metal-based and (e) non-noble metal-based configurations. (f) Voltage profiles of best NMPFs among noble metal-based and non-noble metal-based configurations relative to pristine NVPF, calculated by DFT for validation.

- (4) Building a structure–property space of NMPFs based on ML predictions
- (5) Screening and selecting materials with excellent electrochemical properties
- (6) Validating the proposed materials through DFT calculations

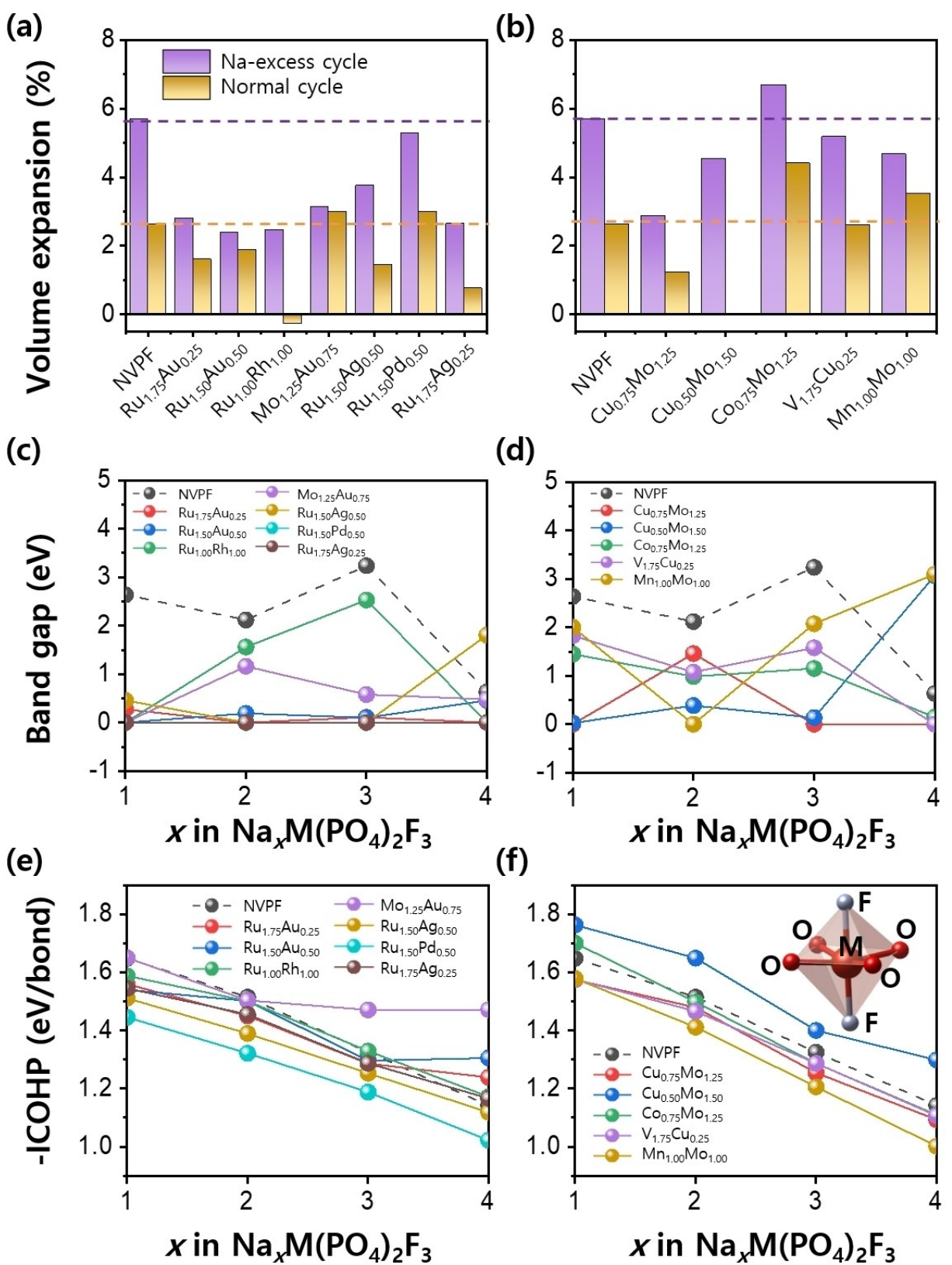


Figure 4. Volume expansion of (a) noble metal-based and (b) non-noble metal-based configurations for assessing cyclability; band gap of (c) noble metal-based and (d) non-noble metal-based configurations for evaluating electronic conductivity; and negative ICOHP of (e) noble metal-based and (f) non-noble metal-based configurations for assessing chemical stability of the proposed NMPF. The results are derived using the proposed GNN model with respect to sodium-ion concentrations. Normal cycle and Na-excess cycle indicate the sodium insertion and extraction processes from Na_1MPF to Na_3MPF and from Na_1MPF to Na_4MPF , respectively. Inset: structural schematic of TM-O-F polyhedral.

3.2. Determination of Atomic Structures of NMPFs and Corresponding DFT Formation Energies

As the first step of the proposed methodology, NMPF structures are generated by replacing vanadium ions with transition metals in the NVPF. The number of element combinations is 465 ($_{30}\text{C}_1 + _{30}\text{C}_2$), incorporating unary and binary compounds in 30 transition metal elements. Considering element ratios (1/7, 2/6, 3/5, 4/4, 5/3, 6/2, and 7/1 for binary compounds in a unit cell with eight TM sites), the overall stoichiometries result in 3,480 compounds. Therefore, 87,870 structures must be calculated due to the different geometrical configurations (atomic arrangements), representing the various possible arrangements of transition metal elements. This reflects the diversity of elemental compositions at each site. To train and test the ML models, the formation energies for 1,171 atomic structures, randomly selected among all structures, are computed through DFT calculations.

3.3. ML Model Construction Using GNN Architectures

Calculating all structures for property space construction requires significant time and resources. Assuming the computation of one structure requires approximately two hours with 68 CPU cores (Intel Xeon Phi 7250 1.4 GHz processor), the calculations for all 87,870 structures would require at least 20 years. However, leveraging the neural network model can reduce the calculation time to a few months. Therefore, we introduce a GNN to predict formation energies from atomic structures. The atomic structures are represented using the crystal graph concept.^[32] The graph format can represent a network composed of points and edges. The GNN models are derived from MEGNet,^[15] pre-trained with the atomic structures and properties specified in the Materials Project database.^[25] The prediction accuracy of our model is enhanced using the atomic structure and property datasets of 1,171 configurations of NMPFs from the original model. The detailed parameters are outlined in the *Methods* Section. The model architecture includes stacked MEGNet blocks, which are collections of dense layers.

To fulfil the requirements of high capacities and voltages, we select structural distortion and voltage levels according to sodium insertion and extraction processes and build two retrained MEGNet (R-MEGNet) models to predict these two properties, named (R-MEGNet-Structure and R-MEGNet-Voltage, respectively, considering various substitution elements and compositions (Figure 2a).

During DFT calculations, structural distortion occurs during structural relaxation when searching for stable structures. This distortion causes the MEGNet model to deviate from the exact formation energies. Notably, MEGNet predicts structures before relaxation, while voltage level calculations use structures after relaxation. Thus, it is reasonable to assume that the energy difference between pre- and post-relaxed structures depends on the degree of the structural distortion, i.e., a larger structural distortion corresponds to a higher energy difference. Therefore,

we consider this energy difference as a measure of the structural distortion and define it as the relaxation energy, $E_{\text{relaxation}}$:

$$E_{\text{relaxation}} = |E_{\text{form}}^{\text{after}} - E_{\text{form}}^{\text{before}}|, \quad (2)$$

where $E_{\text{form}}^{\text{after}}$ and $E_{\text{form}}^{\text{before}}$ are the formation energies of post- and pre-relaxed structures, respectively (Figure S1). While the physical interpretation of relaxation energy may be considered limited due to its dependency on the initial structure, we argue that it holds significance within our framework. This is because the structural stabilities significantly rely on the relaxation energies, making it crucial to predict them for effectively screening stable structures and correcting formation energies.

The Na_0MPF phase is excluded because it is related to the voltage plateau above 4 V and displays excessive structural distortion, which prevents the prediction of formation energies (Figure S2). Moreover, the lattice constants are assumed to be similar to those of the host structures after relaxation. Considering these aspects, we calculate the relaxation energies of 1,171 atomic structures and build the R-MEGNet-Structure models. This model achieves a high accuracy with a correlation coefficient R^2 of 0.961 and a small mean absolute error (MAE) of 0.012. (Figure 2b). As the model accurately predicts the ground truth in the parity plot, R^2 approaches one. Given its satisfactory performance, this model is used for stable structure screening and calibration of formation energies derived from R-MEGNet-Voltage.

According to the Nernst equation, the averaged voltage (V) correlates with the Gibbs free energy change (ΔG) obtained from the total energies.^[33] The total energies of each structure are transformed from the formation energies predicted through the MEGNet. However, the formation energies obtained from the original MEGNet exhibit large errors relative to the DFT results, which are considered the ground truth (Figure S3). These errors are attributable to fact that the original MEGNet yields identical values for different substitution configurations (Figure S4). To address this problem, we retrain the original model with our substituted structure datasets, including different configurations and substitutions. The newly trained model, R-MEGNet-Voltage, achieves a higher accuracy ($R^2 = 0.999$) and lower errors (MAE = 0.00984) compared with the original MEGNet model ($R^2 = 0.866$ and MAE = 0.05563), as shown in Figure 2c, enabling accurate computation of the voltage profile (Figure S5 and Table S1).

3.4. Construction of the Structure–Property Space, Material Screening, and DFT Validation

Using the R-MEGNet-Structure and R-MEGNet-Voltage models, we establish property maps for relaxation energies and voltages (Figures 3a and b). The property maps include 87,870 structures corresponding to 3,480 compounds based on 30 substitutional elements. The voltage levels from Na_4MPF to Na_3MPF , Na_3MPF to Na_2MPF , and Na_2MPF to Na_1MPF are labeled as V_{43} , V_{32} , and V_{21} , respectively.

In the structure–property spaces, 578 compounds from 3,480 compounds are selected based on specific criteria: (1) the variation in relaxation energies is lower than 0.05 eV/atom, determined empirically (Figure S6); (2) the overall voltage profiles have step shapes ($V_{21} > V_{32} > V_{43}$); and (3) V_{21} lies between 3.49 V and 3.90 V. Considering the operating voltage window of 2–4.3 V, V_{43} must be larger than 2 V, and the difference between V_{21} and V_{43} must be small. The screened 578 structures are ranked by the minimum value of $(V_{21}-V_{43})/V_{43}$ (Figure 3c). The top-ranked materials mainly include noble elements, such as Rh, Ru, Pd, Ag, Pt, and Au. These materials are divided into two categories (noble-metal-based and non-noble metal-based NMPFs), given the significance of raw mineral costs in material selection.

Next, predicted voltage profiles of the top-10 noble-metal-based and non-noble metal-based configurations are verified through DFT calculations (Table 1 and Figures 3d and e). The predicted voltage profiles of seven and five materials from the noble-metal-based and non-noble metal-based categories are consistent with the DFT results (Figures S7 and S8). To predict the practical synthesizability of suggested candidate materials, we calculate the crystal-likeness (CL) score using the PU

learning scheme.^[31] Materials with CL scores exceeding 0.5 are considered to be synthesizable, validated against the Materials Project database (Table S2). As summarized in Table 1, all candidates including noble elements are expected to be synthesizable in both pristine and Na-excess compositions, whereas only a few non-noble metal-based candidates are synthesizable. This outcome suggests the advantage of substituting noble elements for synthesizing Na-excess compositions.

Additionally, noble-metal- and copper-containing NMPFs facilitate stable formation of the excess phase and storage of the excess sodium. Details are presented in the *Electronic Supplementary Information*.

3.5. Electrochemical Properties

The cyclabilities, electronic conductivities, and chemical stabilities of the proposed NMPF electrodes are studied by determining the volume expansions, bandgaps, and crystal COHP values.^[27,34,35]

Table 1. Elemental composition, $(V_{21}-V_{43})/V_{43}$, voltage prediction result, and predicted synthesizability of the highest ranking NMPFs with noble metal and non-noble metal-based configurations. Note that M^1 , M^2 , and α correspond to $Na_{0.4}M^{1-\alpha}M^2_\alpha(PO_4)_2F_3$. “○” and “×” in the voltage prediction results indicate whether the voltage profile from DFT satisfies the criteria or not, respectively (voltage profile has a step shape ($V_{21} > V_{32} > V_{43}$), and V_{43} of the NMPFs is higher than that of pristine NVPF). “○” and “×” in the synthesizability results indicates whether the CL core exceeds 0.5 or not, respectively.

Noble metal-based							
Rank	M^1	M^2	α	$(V_{21}-V_{43})/V_{43}$	Voltage Prediction	Synthesizability	
						Na_3MPF	Na_4MPF
1	Fe	Au	0.75	0.141	×	○	○
2	Fe	Au	0.50	0.315	×	○	○
3	Ru	Au	0.25	0.331	○	○	○
4	Ru	Au	0.50	0.334	○	○	○
5	Ti	Pt	1.50	0.352	×	○	○
6	Ru	Rh	1.00	0.379	○	○	○
7	Mo	Au	0.75	0.391	○	○	○
8	Ru	Ag	0.50	0.398	○	○	○
9	Ru	Pd	0.50	0.398	○	○	○
10	Ru	Ag	0.25	0.402	○	○	○
Non-noble metal-based							
Rank	M^1	M^2	α	$(V_{21}-V_{43})/V_{43}$	Voltage Prediction	Synthesizability	
						Na_3MPF	Na_4MPF
1	Cu	Mo	1.25	0.315	○	○	×
2	Cu	Mo	1.50	0.480	○	○	○
3	Ti	Cu	0.50	0.658	×	×	○
4	Co	Mo	1.25	0.666	○	○	×
5	Mn	Tc	1.00	0.675	×	○	○
6	Co	Mo	1.50	0.721	×	○	×
7	V	Cu	0.25	0.740	○	○	×
8	Cu	Ge	1.50	0.750	×	○	×
9	Mn	Ge	1.00	0.786	×	○	×
10	Mn	Mo	1.00	0.834	○	○	×

The cyclability depends on reversible structural variations during charging and discharging (Figures 4a and b). The volume expansion of pristine NVPF is 2.63% for the normal cycle (Na_3VPF to Na_1VPF), which agrees with experimental results of 2.85%,^[5] and increases to 5.69% for the sodium-excess cycle (Na_4VPF to Na_1VPF). Notably, most of the top-ranked NMPFs exhibit smaller volume variations than pristine NVPF.

Bandgaps of NVPF and NMPFs are calculated to assess their electronic conductivities. Pristine NVPF displays a semiconducting bandgap of approximately 3 eV (2.12–3.24 eV) for different sodium concentrations (Na_1VPF – Na_3VPF). In comparison, the sodium-excess phase, Na_4VPF , has a smaller bandgap of 0.63 eV by occupying vanadium $3d\ x^2-y^2$ band (Figure S10). Notably, the proposed NMPFs exhibit considerably smaller bandgaps of about 0.5 eV and about 0.2 eV for $M=\text{Mo}_{1.25}\text{Au}_{0.75}$ and $M=\text{Cu}_{0.5}\text{Mo}_{1.5}$, respectively, compared with pristine NVPF, indicating enhanced conductivity (Figures 4c and d).

To assess the chemical stability, the COHP and integrated COHP (ICOHP) are calculated for the TM-O/TM-F polyhedral, which constitutes the frame of the overall structures (Figures 4e and f and S12). The higher chemical stabilities of NMPFs ($M=\text{Mo}_{1.25}\text{Au}_{0.75}$ and $\text{Cu}_{0.5}\text{Mo}_{1.5}$) compared with pristine NVPF indicate that the proposed NMPFs can withstand volume expansion under reversible cycles and the induced high voltage environment.

4. Conclusions

ML prediction and DFT calculations are combined to identify high-performance SIB cathode materials. Based on the results of the voltage level, cyclability, electronic conductivity, and chemical stability, we theoretically determine $\text{Na}_x\text{Mo}_{1.25}\text{Au}_{0.75}(\text{PO}_4)_2\text{F}_3$ and $\text{Na}_x\text{Cu}_{0.5}\text{Mo}_{1.5}(\text{PO}_4)_2\text{F}_3$ as the most promising cathode materials.

Compared with previous attempts at predicting the voltage level based on deep neural networks, support vector machines, kernel ridge regression,^[36] and CGCNN,^[37] the proposed approach achieve a higher prediction accuracy for the correlation between atomic structures and voltage properties (R^2 : 0.961, MAE: 0.01171 for structural distortion; and R^2 : 0.999, MAE: 0.00984 for formation energy). This improved performance is attributable to the retraining of MEGNet to optimize substituted structures and previously unexplored properties, such as structural distortion and voltage profile. Consequently, the proposed model can identify outstanding materials with greater efficiency and fewer resources compared with direct design approaches. The proposed approach, based on the atomic structure, has a high prediction accuracy and can be applied to diverse materials once target properties, such as structural distortion and voltage level, have been specified. The proposed workflow for systematic, comprehensive, and rapid screening of NASICON-type cathode materials can provide invaluable insights for the development of innovative, high-performance NASICON cathodes.

5. CRediT Authorship Contribution Statement

This manuscript was prepared with the contributions of all authors. All authors have approved the final version of the manuscript. Yoonso Shim, Jong Min Yuk, and Chan-Woo Lee designed the overall work. Yoonso Shim performed DFT calculations, data curation, machine learning, and validation. Incheol Jeong, Junpyo Hur, Hyoungjeen Jeen, Seung-Taek Myung, Seungbum Hong, and Kang Taek Lee evaluated the synthesizability of the proposed materials. Yoonso Shim prepared the manuscript under the supervision of Jong Min Yuk and Chan-Woo Lee.

Acknowledgements

Different aspects of this work were supported by various programs: data curation and inverse design: Korea Advanced Institute of Science and Technology (KAIST)-funded Global Singularity Research Program for 2023, and the National Research Council of Science & Technology (NST) grant by the Korean government (MSIT) (No. CAP22073-000); machine learning and data analysis: National Research Foundation of Korea (NRF) grant funded by MSIP (NRF-2022R1A2C2008929, RS-2023-00222411, and RS-2023-00247245); theoretical calculations: Development Program of Core Industrial Technology funded by the Ministry of Trade, Industry & Energy of Korea (20012318 and 1415186072), and Development of Battery Capacitors for Long-Term, High-Capacity, and High Power Energy Storage System funded by the Ministry of Trade, Industry and Energy (MTIE) and Korea Evaluation Institute of Industrial Technology (Project No: 00155725); synthesizability evaluations: Semiconductor-Secondary Battery Interfacing Platform Technology Development Project of NNFC. Computational resources for this work, i.e., supercomputing resources including technical support, were provided by the National Supercomputing Center (KSC-2020-CHA-0006, KSC-2021-CRE-0140, KSC-2021-CRE-0357, and KSC-2022-CHA-0011).

Conflict of Interests

There are no conflicts to declare.

Data Availability Statement

The data that support the findings of this study are available from the corresponding author upon reasonable request.

Keywords: Na-ion battery • Cathode • NASICON • Inverse design • Graph neural network • Density functional theory

- [1] C. Zhu, C. Wu, C. C. Chen, P. Kopold, P. A. Van Aken, J. Maier, Y. Yu, *Chem. Mater.* **2017**, *29* (12), 5207–5215.
- [2] H. Yi, M. Ling, W. Xu, X. Li, Q. Zheng, H. Zhang, *Nano Energy* **2018**, *47*, 340–352.

- [3] Y. Zhang, S. Guo, H. Xu, *J. Mater. Chem. A* **2018**, *6* (10), 4525–4534.
- [4] X. Liu, G. Feng, E. Wang, H. Chen, Z. Wu, W. Xiang, Y. Zhong, Y. Chen, X. Guo, B. Zhong, *ACS Appl. Mater. Interfaces* **2019**, *11* (13), 12421–12430.
- [5] P.J. Y. ark, Y. Shim, Y. Il Kim, Y. Choi, H. J. Lee, J. Park, J. E. Wang, Y. Lee, J. H. Chang, K. Yim, C. W. Ahn, C. W. Lee, D. K. Kim, J. M. Yuk, *J. Mater. Chem. A* **2020**, *8* (39), 20436–20445.
- [6] W. Liu, H. Yi, Q. Zheng, X. Li, H. Zhang, *J. Mater. Chem. A* **2017**, *5* (22), 10928–10935.
- [7] A. Zunger, *Nat Rev Chem* **2018**, *2* (4), 0121.
- [8] B. Sanchez-Lengeling, A. Aspuru-Guzik, *Science* **2018**, *361* (6400), 360–365.
- [9] K. T. Butler, D. W. Davies, H. Cartwright, O. Isayev, A. Walsh, *Nature* **2018**, *559* (7715), 547–555.
- [10] C. Gao, X. Min, M. Fang, T. Tao, X. Zheng, Y. Liu, X. Wu, Z. Huang, *Adv. Funct. Mater.* **2022**, *32* (1), 2108044.
- [11] C. H. Liow, H. Kang, S. Kim, M. Na, Y. Lee, A. Baucour, K. Bang, Y. Shim, J. Choe, G. Hwang, S. Cho, G. Park, J. Yeom, J. C. Agar, J. M. Yuk, J. Shin, H. M. Lee, H. R. Byon, E. Cho, S. Hong, *Nano Energy* **2022**, *98*, 107214.
- [12] S. Hong, C. H. Liow, J. M. Yuk, H. R. Byon, Y. Yang, E. Cho, J. Yeom, G. Park, H. Kang, S. Kim, Y. Shim, M. Na, C. Jeong, G. Hwang, H. Kim, H. Kim, S. Eom, S. Cho, H. Jun, Y. Lee, A. Baucour, K. Bang, M. Kim, S. Yun, J. Ryu, Y. Han, A. Jetbybayeva, P.-P. Choi, J. C. Agar, S. V. Kalinin, P. W. Voorhees, P. Littlewood, H. M. Lee, *ACS Nano* **2021**, *15* (3), 3971–3995.
- [13] T. Xie, J. C. Grossman, *Phys. Rev. Lett.* **2018**, *120* (14), 145301.
- [14] S. Sanyal, J. Balachandran, N. Yadati, A. Kumar, P. Rajagopalan, S. Sanyal, P. Talukdar, *arXiv preprint arXiv:1811.05660* **2018**.
- [15] C. Chen, W. Ye, Y. Zuo, C. Zheng, S. P. Ong, *Chem. Mater.* **2019**, *31* (9), 3564–3572.
- [16] D. Jha, L. Ward, A. Paul, W. Liao, W. keng, A. Choudhary, C. Wolverton, A. Agrawal, *Sci. Rep.* **2018**, *8* (1), 17593.
- [17] S. Y. Louis, Y. Zhao, A. Nasiri, X. Wang, Y. Song, F. Liu, J. Hu, *Phys. Chem. Chem. Phys.* **2020**, *22* (32), 18141–18148.
- [18] C. W. Park, C. Wolverton, *Phys. Rev. Mater.* **2020**, *4* (6) 063801.
- [19] K. Das, B. Samanta, P. Goyal, S. C. Lee, S. Bhattacharjee, N. Ganguly, *NPJ Comput Mater* **2022**, *8* (1), 43.
- [20] Z. Ahmad, T. Xie, C. Maheshwari, J. C. Grossman, V. Viswanathan, *ACS Cent. Sci.* **2018**, *4* (8), 996–1006.
- [21] V. B. Shenoy, N. C. Frey, D. Akinwande, D. Jariwala, *ACS Nano* **2020**, *14* (10), 13406–13417.
- [22] G. Kresse, J. Furthmüller, *Phys. Rev. B* **1996**, *54* (16), 11169–11186.
- [23] J. P. Perdew, K. Burke, M. Ernzerhof, *Phys. Rev. Lett.* **1996**, *77* (18), 3865–3868.
- [24] H. J. Monkhorst, J. D. Pack, *Phys. Rev. B* **1976**, *13* (12), 5188–5192.
- [25] A. Jain, S. P. Ong, G. Hautier, W. Chen, W. D. Richards, S. Dacek, S. Cholia, D. Gunter, D. Skinner, G. Ceder, K. A. Persson, *APL Mater* **2013**, *1* (1), 011002.
- [26] M. Lee, Y. Youn, K. Yim, S. Han, *Sci. Rep.* **2018**, *8* (1), 14794.
- [27] S. Maintz, V. L. Deringer, A. L. Tchougréeff, R. Dronskowski, *J. Comput. Chem.* **2013**, *34* (29), 2557–2567.
- [28] F. Chollet, et al., *Keras* **2015**.
- [29] M. Abadi, A. Agarwal, P. Barham, E. Brevdo, Z. Chen, C. Citro, G. S. Corrado, A. Davis, J. Dean, M. Devin, S. Ghemawat, I. J. Goodfellow, A. Harp, G. Irving, M. Isard, Y. Jia, R. Józefowicz, L. Kaiser, M. Kudlur, J. Levenberg, D. Mané, R. Monga, S. Moore, D. G. Murray, C. Olah, M. Schuster, J. Shlens, B. Steiner, I. Sutskever, K. Talwar, P. A. Tucker, V. Vanhoucke, V. Vasudevan, F. B. Viégas, O. Vinyals, P. Warden, M. Wattenberg, M. Wicke, Y. Yu, X. Zheng, *arXiv* **2016**, abs/1603.04467.
- [30] F. Pedregosa, *J Mach Learn Res* **2011**, *12*, 2825–2830.
- [31] J. Jang, G. H. Gu, J. Noh, J. Kim, Y. Jung, *J. Am. Chem. Soc.* **2020**, *142* (44), 18836–18843.
- [32] T. Xie, J. C. Grossman, *Phys. Rev. Lett.* **2018**, *120* (14), 145301.
- [33] G. Yoon, D. H. Kim, I. Park, D. Chang, B. Kim, B. Lee, K. Oh, K. Kang, *Adv. Funct. Mater.* **2017**, *27* (40).
- [34] R. Dronskowski, P. E. Blochl, *J. Phys. Chem.* **1993**, *97* (33), 8617–8624.
- [35] V. L. Deringer, A. L. Tchougréeff, R. Dronskowski, *J. Phys. Chem. A* **2011**, *115* (21), 5461–5466.
- [36] R. P. Joshi, J. Eickholt, L. Li, M. Fornari, V. Barone, J. E. Peralta, *ACS Appl. Mater. Interfaces* **2019**, *11* (20), 18494–18503.
- [37] X. Zhang, J. Zhou, J. Lu, L. Shen, *NPJ Comput Mater* **2022**, *8* (1) 175.

Manuscript received: March 30, 2024

Accepted manuscript online: April 16, 2024

Version of record online: July 3, 2024